energies

MDPI

Article

Investigating the Performance of a Super High-head Francis Turbine under Variable Discharge Conditions Using Numerical and Experimental Approach

Zheming Tong [1,2,*], Hao Liu [1,2], Jianfeng Ma [3], Shuiguang Tong [1,2,*], Ye Zhou [4], Qiang Chen [5] and Yunzhe Li [3]

1 State Key Laboratory of Fluid Power and Mechatronic Systems, Zhejiang University, Hangzhou 310027, China
2 School of Mechanical Engineering, Zhejiang University, Hangzhou 310027, China
3 Zhejiang Fuchunjiang Hydropower Equipment Co., Ltd., Hangzhou 311121, China
4 China Institute of Water Resources and Hydropower Research, Beijing 100038, China
5 China Gezhouba Group Mechanical & Electrical Construction Co., Ltd., Chengdu 610000, China
* Correspondence: tzm@zju.edu.cn (Z.T.); cetongsg@zju.edu.cn (S.T.)

Received: 22 May 2020; Accepted: 16 July 2020; Published: 29 July 2020

Abstract: A super high-head Francis turbine with a gross head of nearly 700 m was designed with computational fluid dynamics (CFD) simulation and laboratory tests. Reduced-scale (1:3.7) physical and numerical models of the real-scale prototype were created to investigate the hydraulic performance. According to the CFD analysis, a strong rotor–stator interaction (RSI) between guide vanes and runner blades is observed as a result of the high-speed tangential flow towards runner created by the super high water head as well as the small gaps between the radial blades. At the designed best efficiency point (BEP), there is no significant flow recirculation inside the flow passage and minor loss occurs at the trailing edge of the stay vanes and guide vanes. Maximum velocity is observed at runner inlets due to flow acceleration through the narrow passages between the guide vanes. The elbow-shaped draft tube gradually decreases the flow velocity to keep the kinetic energy loss at a minimum. The laboratory test was conducted on a reduced-scale physical model to investigate the pressure pulsations and guide vane torque (GVT) under variable-discharge configurations, which are key concerns in the design of a high head turbine. Pressure sensor networks were installed at the inlet pipe, vaneless space and draft tube, respectively. The most intense pressure variation occurs at the inlet pipe and elbow at 0.04–0.2 GVO_{BEP} and 1.5–1.8 GVO_{BEP} with a low frequency about 0.3 times of the runner frequency, while the vibration in vaneless zone performs stable with the blade passing frequency caused by RSI. The GVT shows a declining trend and then keeps stable as GVOs increases at synchronized condition. For the misaligned conditions, the torque of adjacent guide vanes differs a lot except at the synchronous angle and maximum absolute value at least doubles than the synchronized condition.

Keywords: Francis turbine; super high-head; pressure pulsation; guide vane torque; hill chart

1. Introduction

Nowadays, renewable energy plays a great role in world's energy system. Hydropower as a key component of renewable energy shows several advantages against others such as wind and solar. First, hydropower has the best conversion efficiency among a variety of energy sources, reaching 95% in certain types of Francis turbines [1]. Second, intermittent renewable energy such as solar and wind is difficult to fully integrate into the power system due to stability issues. Third, the cost of hydroelectricity is much lower than other renewables, which makes it a very competitive source of

renewable electricity. Hydropower is a proven and well-advanced technology based on more than a century of experience, and has been a driving force for many countries to adjust their energy structure and deal with the threat of global warming and environmental pollution.

Francis turbines are the most widely used turbine type around the world due to the relatively compact structure, high operation efficiency, and wide range of water heads. Normally, the Francis type is operated under the water head from 100 to 300 meters to achieve the highest energy conversion efficiency with 90–95% [2]. In recent years, many large-scale hydropower projects such as the Baihetan Dam and Xiluodu Dam projects have been constructed in China. The remaining undeveloped water resources are mainly distributed in the western mountainous areas of China [3]. Francis turbines are commonly operated under off-design operations to balance the real-time load change in a huge grid network [4]. To meet the demand above, a new type of Francis turbine has been developed with a super high water head (over 400 m) and large capacity. However, such a type of design for a specific set of conditions running at a particular scenario has generally become more challenging, although some earlier successful projects have been provided [5], as illustrated in Table 1. The increased water head causes growing pressure at the turbine locations, and the turbine size must be reduced to adapt to the given flow conditions. Besides, the rated speed and flow velocity of high-head Francis turbine both are higher than the low-head ones, resulting in a larger impact force on the blades. These obstacles all increase the difficulty in design and manufacturing, which slows down the development of super high-head Francis turbines in China.

Table 1. The representative high-head Francis turbines in the world.

Power Station/Country	Year	Rated Head (m)	Rated Power (MW)	Rated Speed (r/min)	Specific Speed (m·kw)	Runner Diameter (m)
Sorfjord, Norway	1980	585	60	750	63.9	1.06
Holen, Norway	1984	610	154	500	64.7	1.61
Häusling, Austria	1986	734	181	600	70.3	2.767
Koyna, India	1994	525	255	375	75.4	2.40
Yaoji, China	2006	490	82.1	600	74.6	1.30
Jianke, China	Under construction	495	83.67	600	74.3	—

Computational fluid dynamics (CFD) and laboratory test are combined to develop a super high head Francis turbine. CFD allows a quick and efficient preliminary design of machine components [6–8]. Flow patterns become highly complex under off-design conditions, and existing models cannot fully capture the complicated unsteady flow phenomenon [9,10]. CFD-based methodologies must be validated through experimental data [11,12]. Therefore, the laboratory test is an indispensable means in hydraulic turbine design. Normally, the experiment of the model is carried out for forecasting prototype turbine performance using a reduced-scale turbine [13], which provides a valuable reference for the calibration of the hydrodynamic calculation and the comparison of different design schemes.

Existing numerical and experimental studies have been conducted to investigate the performance characteristics in Francis turbine over past decade, as summarized in Table 2. Some researchers focused on the single operating condition comprising deep part load (DPL), part load (PL), best efficiency point (BEP), high load (HL) and full load (FL). Some studies characterized the turbine performance in a wide operation range or transient process [14–17]. At present, researchers have reached a consensus on many aspects. The hydrodynamics instabilities in Francis turbine can lead to significant vibrations, abnormal operations of the unit or even the unplanned stop during off-design operations [18,19]. At PL condition, the flow downstream the runner can promote the formation of a vortex core in the draft tube with a low frequency about 0.3–0.5 times of the runner rotational speed. If the value matches the natural frequencies of the hydraulic unit structure, uncontrolled resonance and obvious vibrations may transpire [20]. At full load, the pressure oscillations translate into dangerous electrical power swings, whose peak-to-peak amplitude can reach up to 5–10% of the rated power [21]. To improve the flow stability and minimize pressure pulsations, some measures have been taken: misaligned guide vanes (MGVs) have, to date, been exclusively incorporated in the pump-turbine system [22]. As the most intuitive characterization of hydraulic turbines, the hill chart provides details pertaining

to performance under various guide vane openings (GVOs), hydraulic efficiency, water head, power output and discharge conditions [23]. However, this may be a time and cost consuming work. For the confidentiality of power plants, there are few works in the literature to promulgate the details. Trivedi et al. [24] introduced the Francis-99 platform and disclosed the design parameters and experiment data of the Francis-99 model turbine, which provides the possibility of mutual verification in the hydraulic turbine industry.

Table 2. Summary of studies on hydro-turbine with computational fluid dynamics (CFD) and experiment (ordered by publish date).

Reference	Year	Condition	Method	Study
[25]	2009	PL (0.87Q_{BEP})	experimental survey	pressure fluctuations
[26]	2010	FL	site measurement and SST	vortex rope; pressure
[27]	2012	startup phase	k-e model	flow physics
[28]	2013	optimum and off design conditions	site test and k-ω SST model	CFD design
[29]	2015	PL and HL	DES	pressure pulsations
[30]	2016	PL to FL (0.2 1Q_{max})	CFD, experiment and ANN	CFD and experimental design
[31]	2016	Runaway	SAS-SST model	flows and pressure
[32]	2016	PL	site measurement and SAS-SST model	structural analysis
[33]	2016	PL	RNG k-ε turbulence model	MGVs
[34]	2017	DPL (0.27 Q_{BEP})	BSL-EARSM model	pressure; vortices
[35]	2017	DPL (0.2–0.5 Q_{BEP}) PL (0.5–0.8 Q_{BEP})	visualization, SAS-SST, k-ω SST model	cavitation flows; vortex
[21]	2017	FL (1.3 Q_{BEP})	visualization	instability in DT
[36]	2017	PL	site measurement and SAS-SST model	load spectra
[37]	2018	speed-no-load	four URANS models	the turbulence model
[38]	2019	PL	SST-SAS	synchronous pressure fluctuations
[39]	2019	speed-no-load to FL	site measurement and SBES model	fatigue analysis

Giving a summary of the above literature, most studies focus on PL condition rather than HL condition [40]. The performance of high-head Francis turbine under different GVOs from PL to HL is included, while fewer DPL and FL conditions are described in one study. Besides, the vibrational performance and its physical origins of high-head Francis turbines are quite complex and have not been fully investigated to date, especially in DPL and FL conditions. From the perspective of research objects, the existing literature focuses on mostly regular Francis turbines, super high-head Francis turbines has not been investigated before. How to design a super high-head Francis turbine and understand the differences and similarities from other types of Francis turbines are of great research importance.

In this study, we presented the development of a super high-head Francis turbine with a gross head of nearly 700 m with CFD simulation and laboratory tests. The objective of this study is to discuss several key aspects for designing a super high-head Francis turbine with a maximum water head nearly 700 m. The paper is organized as follows. Section 2 describes the details of the numerical and experimental setup. Section 3 presents the results and discussions of the model and prototype turbine. Key findings and observations are provided in Section 4.

2. Methodology

2.1. Design of Super High-Head Runner of Francis Turbine

For a super high-head hydropower station, the runner is the heart of the turbine where water power is transformed into the rotational force that drives the generator. The hydraulic performance was investigated with CFD and laboratory test, as shown in Figure 1. First, based on the site characteristics of the hydropower station and the demand of the user, the specific speed, rotational speed, and power output of the prototype turbine were determined by a set of parameters, such as the gross head, rated net head, unit discharge, the desired operating range. The geometry of a preliminary runner and its hill chart were created based on similarity theory and in-house runner database that contains a wide range of

existing runners from past projects. Second, a CFD-based multi-objective optimization was conducted to fine-tune the hydraulic performance of the preliminary runner design. The objective function was defined to address minimum losses and maximum efficiency at the design point. The blade's geometry was parameterized using NURBUS curves and surfaces. Once an optimized runner was obtained in CFD, a physical runner model was created to validate the results from the simulation. Lastly, if the experimental results of laboratory tests were not in good agreement, the CFD-based optimization will be repeated until the results become satisfactory.

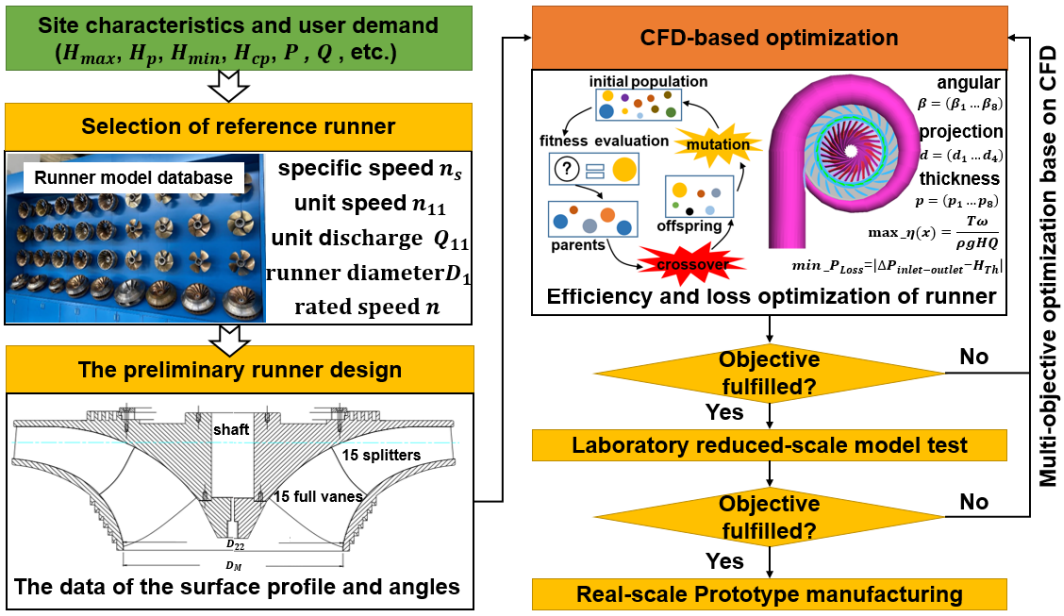

Figure 1. The design process of the super high-head Francis turbine.

The final design of the prototype is shown in Figure 2, the rated flow rate, output and speed are 21.3 m^3/s, 126 MW and 600 rpm, respectively. Thus the specific speed n_s is calculated to be 64.27. The specific speed coefficient K is 1644.9. The runner outlet diameter of the prototype is 1300 mm. The turbine includes a runner with 15 full blades and 15 splitters in an alternate arrangement, 23 stay vanes equally distributed along the centerline, 23 guide vanes, a spiral casing with 24 sections, and an elbow draft tube. X-shaped blades are adopted for the runner.

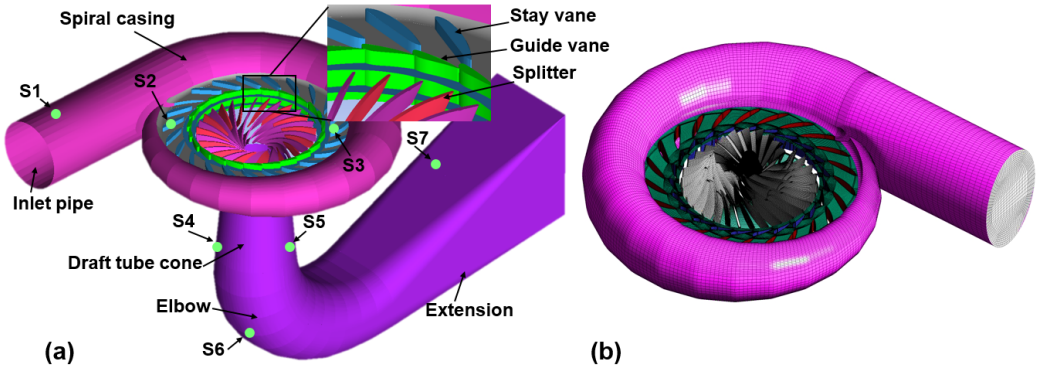

Figure 2. (**a**) The Francis turbine model. Pressure sensor network was installed to measure the pressure pulsations, the locations were recommended by the International Electrochemical Commission (IEC) standard. Sensor S1 was mounted at the inlet pipe. S2 and S3 were on the upper cover between guide vanes and runner. S4 and S5 were located on the surface of the draft tube cone, S6 and S7 were arranged to monitor the draft tube bend and extension, respectively; (**b**) The meshes of the calculation domain.

2.2. Numerical Method

A reduced physical model (1:3.7) of the real-scale prototype was created in CFD. The runner outlet diameter is 350 mm. The whole turbine passage from the inlet of the spiral case to the outlet of the draft tube was adopted as the computing domain. The components were discretized with structured hexahedral meshes using a blocking method (Figure 2b). The grid independence test derived an optimal mesh size of 6.5 million elements where the variation in torque of the last two tested grid sizes was less than 5% at BEP. Wall function was used to approximate the near-wall boundary layer, which substantially reduced the effort to explicitly resolve the boundary layer. The average values of y plus obtained in the spiral casing, runner and draft tube domain were 85, 64.5, and 95, respectively. The steady-state incompressible flow simulation was carried out with the flow solver. The Multiple Reference Frame Model (MRF) was applied to model the stator-rotor interaction. The calculated data were transferred through the interface pairings. The runner was described in the rotating reference frame, and the flow in the stationary components was treated as the stationary frame of reference. The pressure type boundary was set at the inlet of spiral casing. A free outflow of total mass flow rate was given at the draft tube outlet. The direction of outlet velocity was set as normal to the boundary. A no-slip wall setup was applied on all solid walls. The method of pressure–velocity coupling was realized using the SIMPLE algorithm and the second-order upwind scheme was applied for the spatial discretization except for pressure terms with the PRESTO program. Re-Normalization Group (RNG) k-ε model was selected as the turbulence model due to the better performance compared to the standard k-ε model when dealing with the high streamline curvature and strain rates, the transport equations of turbulence kinetic energy k and its dissipation rate ε are defined as

$$\frac{\partial}{\partial t}(\rho k) + \frac{\partial}{\partial x_i}(\rho k u_i) = \frac{\partial}{\partial x_j}\left[\left(\upsilon + \frac{\mu_t}{\sigma_k}\right)\frac{\partial k}{\partial x_j}\right] + P_k - \rho\varepsilon \tag{1}$$

$$\frac{\partial}{\partial t}(\rho \varepsilon) + \frac{\partial}{\partial x_i}(\rho \varepsilon u_i) = \frac{\partial}{\partial x_j}\left[\left(\upsilon + \frac{\mu_t}{\sigma_\varepsilon}\right)\frac{\partial \varepsilon}{\partial x_j}\right] + C_{1\varepsilon}\frac{\varepsilon}{k}P_k - C^*_{2\varepsilon}\rho\frac{\varepsilon^2}{k} \tag{2}$$

where u_i is the velocity component in i direction, $C^*_{2\varepsilon} = C_{2\varepsilon} + C_\mu\eta^3(1-\eta/\eta_0)/\left(1+\beta\eta^3\right)$, $\eta = Sk/\varepsilon$, $S = \sqrt{2S_{ij}S_{ij}}$, $\eta_0 = 4.38$, $C_{1\varepsilon} = 1.42$, $C_{2\varepsilon} = 1.68$, $C_\mu = 0.0845$, $\beta = 0.012$. The quantities σ_k and σ_ε are the inverse effective Prandtl numbers for k and ε, respectively, with both 0.07194.

2.3. Experiment Setup

2.3.1. Laboratory Test and Calibration

In this study, the investigated Francis turbine is a reduced physical model (1:3.7) of the real-scale prototype, which is geometrically identical to the prototype but reduced in size. The test circuit can be operated either with a closed or open loop according to the measurement types. In turbine mode, the water is pumped through the flow meters to the high head tank and further through the model to the low head tank. From the low head tank, the water flows into the return pipeline and the reservoir. A water cooler is installed in the pipeline to keep the temperature stable. The discharge of the turbine is regulated by the GVOs. The water head varies with the selected speed of the reversible pump turbine. The gantry carries the load of the test rig equipment, such as high head and low head tanks, the dynamometer and the model platform.

The instrumentation, calibration, measurement procedure, and data analysis are performed in accordance with the relevant standards IEC 60193 [41] and ISO 4185 [42]. The electrical and oil hydraulic units were operated with a programmable logic controller (PLC) system. The hardware consists of a National Instruments data acquisition system (DAQ-system). The water discharge was measured with an electromagnetic flowmeter calibrated with a weighing tank system. The torque was computed from the measurement of dynamometer and friction transducer load and was calibrated by applying class M2 weights. A rotary encoder was mounted on the generator shaft to obtain rotational

speed. The speed signal was connected to the Frequency Reference Standard during calibration. The GVOs measuring system consists of an absolute rotary encoder mounted on the shaft and no need for calibration. Pressure pulsations were measured by seven piezoelectric pressure transducers, which were calibrated by applying a known gas pressure. The observations of the draft tube cone were made with the use of a camera.

The total uncertainty was quantified as the root-sum-square of the systematic and random uncertainties in Equation (3). The random uncertainties were stated at a 95% confidence level. The systematic errors were assessed using information from the certificates, the calibration history of the instrument and the cumulative effect through the calibrations, specifically including torque (e_T), discharge (e_Q), head (e_H) and runner rotational speed (e_n) in Equation (4). The combined uncertainty was calculated to be ±0.22% at 25 m test head according to Table 3.

$$e_{total} = \sqrt{{e_r}^2 + {e_s}^2} \tag{3}$$

$$e_s = \sqrt{{e_T}^2 + {e_Q}^2 + {e_H}^2 + {e_n}^2} \tag{4}$$

Table 3. The obtained uncertainties in the flow measurement through the calibrations.

Parameter	Systematic Uncertainty e_s (%)	Random Uncertainty e_r 95 (%)
torque	±0.12	±0.06
head	±0.08	±0.03
discharge	±0.12	±0.09
speed	±0.005	±0.005
total	±0.19	±0.11

2.3.2. Similarity Theory

The specific hydraulic energy for the model is defined by

$$E_M = \frac{P_{abs,1} - P_{abs,2}}{\overline{\rho}} + \frac{v_1^2 - v_2^2}{2} \tag{5}$$

where P_{abs} is the static pressure, $\overline{\rho}$ is the average density of upstream and downstream, written as $\overline{\rho} = (\rho_{M1} + \rho_{M1})/2$, ρ_{M1} and ρ_{M2} are the water density at the high and low pressure side. v is the flow velocity, subscripts 1 and 2 represent the high and low pressure side, respectively.

The net pressure P_M, model net head H_M, hydraulic power P_{hM} available for producing power on the model and mechanical power P_{mM} are given by Equations (6)–(9), respectively. The hydraulic efficiency of the model η_{hM} is calculated based on the ratio of P_{mM} to P_{hM}, which is described in Equation (10).

$$P_M = E_M \rho_M \tag{6}$$

$$H_M = \frac{E_M}{g_M} \tag{7}$$

$$P_{hM} = E_M \rho_{M1} Q_M \tag{8}$$

$$P_{mM} = \frac{\pi n_M}{30}\left(r_d g_M (m_c + m_L) + r_f g_M m_f\right) \tag{9}$$

$$\eta_{hM} = \frac{P_{mM}}{P_{hM}} \tag{10}$$

where g_M is the gravity acceleration, Q_M is the model discharge, n_M is the rotational speed of the model, r_d is the length of the dynamometer lever arm, r_f is the length of the friction lever arm, m_c is the dynamometer transducer load, m_L is mass of fixed weights on dynamometer, m_f is friction transducer load.

Dimensionless factors of speed, discharge and power are described as Equations (11)–(13), respectively.

$$n_{ED} = \frac{n_M D_M}{60 E_M^{0.5}} \tag{11}$$

$$Q_{ED} = \frac{Q_M}{D_M^2 E_M^{0.5}} \tag{12}$$

$$P_{ED} = \frac{P_{mM}}{\rho_{M1} D_M^2 E_M^{1.5}} \tag{13}$$

where n_M is the runner rotational speed in revolutions per minute, D_M is the diameter of the model runner.

In general, prototype performance is estimated by using the scaling technology in the design stage, so-called similarity laws [43,44]. Experimental conditions, i.e., Reynolds number, specific energy and reference diameter all fulfill the International Electrotechnical Commission (IEC) requirements. Prototype specific energy E_P, prototype discharge Q_P, prototype mechanical power P_{mP} and prototype guide vane torque T_{GPX} are scaled by Equations (14)–(17).

$$E_P = E_M \left(\frac{D_P}{D_M}\right)^2 \left(\frac{n_P}{n_M}\right)^2 \tag{14}$$

$$Q_P = Q_M \left(\frac{D_P}{D_M}\right)^3 \frac{n_P}{n_M} \tag{15}$$

$$P_{mP} = P_{mM} \frac{\eta_{hM}}{\eta_{hP}} \left(\frac{D_P}{D_M}\right)^5 \left(\frac{n_P}{n_M}\right)^3 \left(\frac{\rho_P}{\rho_M}\right) \tag{16}$$

$$T_{GPX} = T_{GMX} \left(\frac{D_P}{D_M}\right)^3 \left(\frac{\rho_P}{\rho_M}\right) \left(\frac{E_P}{E_M}\right) \tag{17}$$

where T_{GMX} is the torque on guide vane number x of the model.

The model hydraulic efficiency measured in the experiment will be scaled up to prototype efficiency at prototype Reynolds number with the two-step method. The relation is written:

$$\begin{cases} \eta_{hM^*} = \eta_{hM} + (\Delta\eta_h)_{M \to M^*} \\ \eta_{hP} = \eta_{hM^*} + (\Delta\eta_h)_{M^* \to P} \end{cases} \tag{18}$$

where the difference between the model and prototype efficiency is expressed as

$$\begin{cases} (\Delta\eta_h)_{M \to M^*} = \delta_{ref} \left[\left(\frac{Re_{ref}}{Re_M}\right)^{0.16} - \left(\frac{Re_{ref}}{Re_{M^*}}\right)^{0.16} \right] \\ (\Delta\eta_h)_{M^* \to P} = \delta_{ref} \left[\left(\frac{Re_{ref}}{Re_{M^*}}\right)^{0.16} - \left(\frac{Re_{ref}}{Re_P}\right)^{0.16} \right] \end{cases} \tag{19}$$

where η_{hM^*} is the nominal hydraulic efficiency of the model, δ_{ref} is hydraulic efficiency convertible loss rate, Re_{ref} is reference Reynolds number referring to 7×10^6, Re_M is model Reynolds number at the actual experimental point, Re_P is prototype Reynolds number.

3. Results and Discussion

3.1. Simulation Analysis

A key characteristic of Francis turbine is that flows change directions as they pass through the volute casing and runner. The uniform distribution of the flows around the runner is significant for the balanced operation of the turbine. Figure 3a shows the relative energy loss from the inlet scaled to

the unit discharge $Q_{11}^2 = 1$. The outflow from the spiral casing matches well with the inflow toward stay vanes without any flow separation and bad flow patterns throughout the passageways. The only minor loss occurs at the trailing edge of the stay vanes due to the wakes. Figure 3b depicts the pressure distribution on central plane of spiral casing. The pressure is distributed evenly around the casing and decreases towards the runner. There is no obvious abnormal pressure drop due to the flow recirculation. The lowest pressure is observed at the narrow space between the baffle plate and last stay vane.

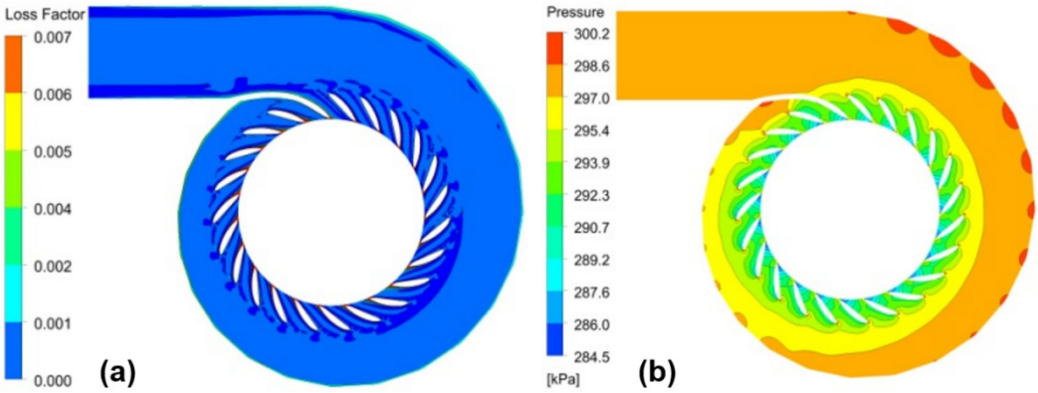

Figure 3. The contour plots at the mid plane of the spiral casing and stay vanes at BEP condition. (**a**) The energy loss factor from the inlet scaled to $Q_{11}^2 = 1$, expressed as $(E_{inlet} - E_i)/E_{inlet}$, E_{inlet} and E_i are the total energy at inlet and local position, respectively; (**b**) The calculated pressure at the mid-plane of the spiral casing.

Figure 4a shows the flow angles in the passage upstream the draft tube, which displays a great flow match between different turbine components. The radial and circumferential components of incoming flows from the penstock pipe gradually increase in spiral casing. The water then is distributed evenly through the periphery of the stay ring. The flow around the stay vanes was reflected by its angle at inlet and outlet, as shown in Figure 4b,c. Flow angles display periodicity in the circumferential direction on the whole, although remarkable disparities exist. Some vicious cycles of bad inflow angles are observed. The first stay vane experiences quite uniform inflow. From 4# stay vane, the secondary flows created by the curving spiral casing increase the flow angles near the stay rings, leading to the same performance of adjacent stay vanes. When the flow leaves the stay vanes, most of the deviating flow angles at the inlet have been corrected and the flow distribution is very uniform. The flow angles at different Z levels indicate that they vary with the stay vanes height. Upper flows deviate more easily than that in lower locations. This may be due to the higher pressure near the bottom, where the flow is not easy to disperse, always along the surface profile of the stay vanes.

A typical flow field around guide vanes and runner is shown in Figure 5a with a blade-to-blade view. The operational point is the BEP with an n_{11} corresponding to a net head of 640 m. The water is accelerated sharply in the guide vanes cascade, resulting in a high-velocity stream of flow with about 15 m/s distributed in the narrow passages adjacent to the high-speed rotating runner, where the stronger rotor–stator interaction occurs compared with other conventional Francis turbines with a relatively larger buffer interval between guide vanes and runner inlet. This is one of the most noteworthy issues in the design of super high-head Francis turbines. The higher velocity can be observed at the suction side than the pressure side. The minimum velocity region appears at the chamfered leading edge of impeller blades, where experiences the flow detachment. Figure 5b presents the pressure distributions at the runner and guide vanes. The pressure is high as the flow advances before the guide vanes, whereas it drops obviously at runner inlet as a result of the accelerated jets toward the runner, and it decreases continuously along with the runner blades due to the torque transfer and flow direction transformation. A smooth pressure transition is observed inside the interblade passage with the desirable straight contour lines, avoiding the cross flows from high to low pressure regions. The results

indicate that the inflow matches well with the metal angles of the runner blades, which are designed to cope with different inflow angles due to variations in both flow discharge and net head. With such a design and a correct position of the inlet edge from band to hub together with the splitter vanes, the losses and appearances of vortices are minimized.

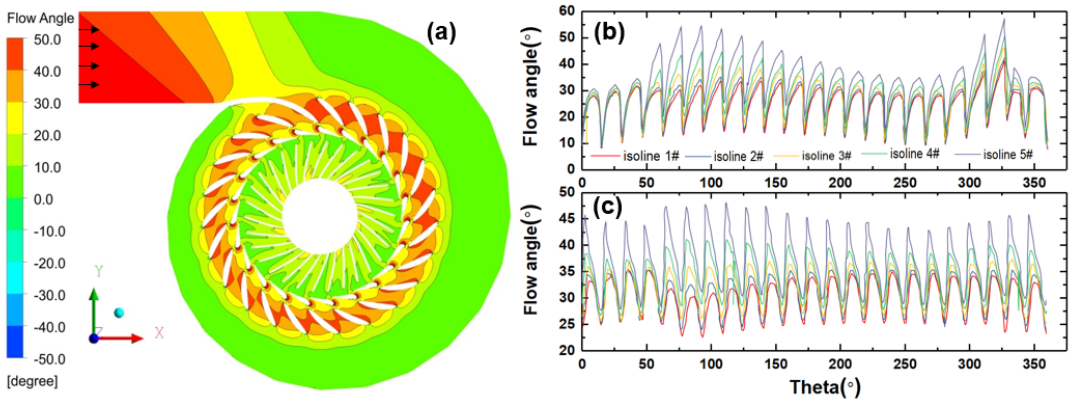

Figure 4. (**a**) The flow angles from the spiral casing inlet to the runner outlet at BEP, which are calculated as $\tan^{-1}(v_r/v_t)$, v_r and v_t are the axial and tangential velocity components, respectively; (**b**) The inlet flow angles towards the stay vanes from spiral casing; (**c**) The flow angles leaving out of the stay vanes. The flow swirls in spiral casing from the 1# stay vane to 23# stay vane, which means the theta varies from 0° to 360°. The height of a stay vane was divided into five parts equally, the bottom line is defined as isoline 1.

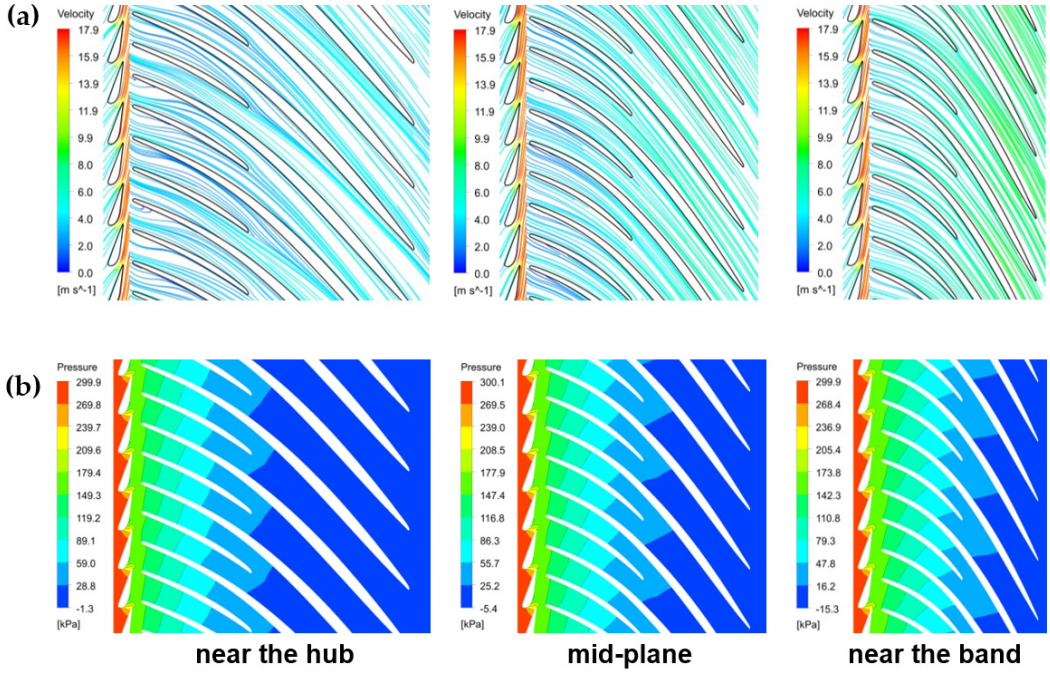

Figure 5. The blade-to-blade view of velocity streamlines (**a**) and pressure contours (**b**) at different slices of runner and guide vanes, which are near the hub, mid-plane and near the band, respectively.

Figure 6 presents the streamlines and pressure in the draft tube at BEP, the color of the streamlines denotes the velocity of the flow. A slender stationary swirling structure is observed along the axis centerline of the draft tube due to the existing radial component of velocity at runner outlet, higher velocities and larger velocity gradients occur in the vortex center. It gradually decays as it gets closer to the elbow and outlet. A low-pressure area is observed below the runner hub and quickly

disappears downstream to the elbow. The pressure in elbow outside is nearly twice as that in inside. The pressure recovers in rectangular diffuser where the retained kinetic energy is converted into the static pressure successfully.

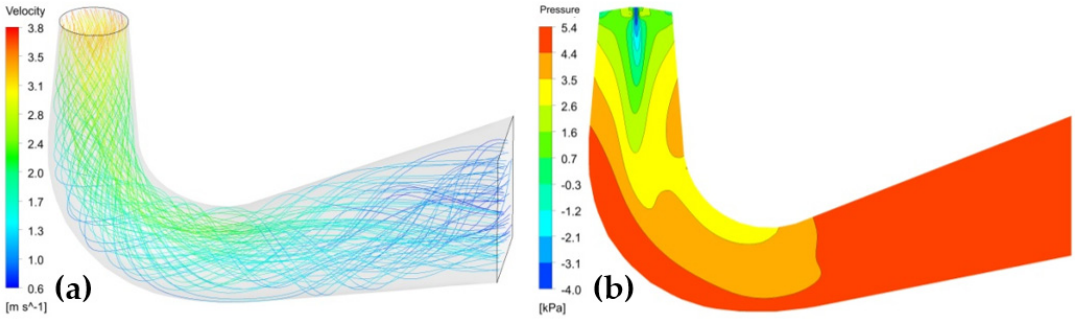

Figure 6. Velocity streamlines (**a**) and pressure contour (**b**) at draft tube.

3.2. *Analysis of Experiment Results*

3.2.1. Comprehensive Characteristic Curve

Figure 7 displays the Hill diagram of the reduced-scale (1:3.7) Francis turbine, which was constructed based on 380 operating points, specifically including 19 different positions of guide vanes and 20 repetitions of the runner angular speed made for each GVOs. The BEP of the model turbine was recorded at GVOs $= 10.6°$, where the optimum hydraulic efficiency corrected to Re $= 7 \times 10^6$ is 93.53%, whereas the CFD-simulated efficiency at BEP is 94.62%. A close agreement between CFD and experimental test was observed. The deviation is likely due to the ignore of sidewall gaps and disc friction. n_{ED} and Q_{ED} are equal to 0.164 and 0.134, respectively. The unit values n_{11} and Q_{11} are equal to 30.9 rpm and 0.419 m^3/s. The prototype Reynolds number is calculated to be 5.034×10^6 at runner speed 600 rpm and water temperature 18°C, the scalable losses δ_{ref} and the scale-up efficiency $(\Delta\eta_h)_{M^* \to P}$ are 0.0453 and 1.66%, respectively. Thus the scaled-up maximum prototype hydraulic efficiency at nominal condition is calculated to be 94.75% at net head 639.8 m. The Hill diagram then was applied in the further more research and development of new type design of prototype turbine based on quick comparison and evaluation of the minor improvement design.

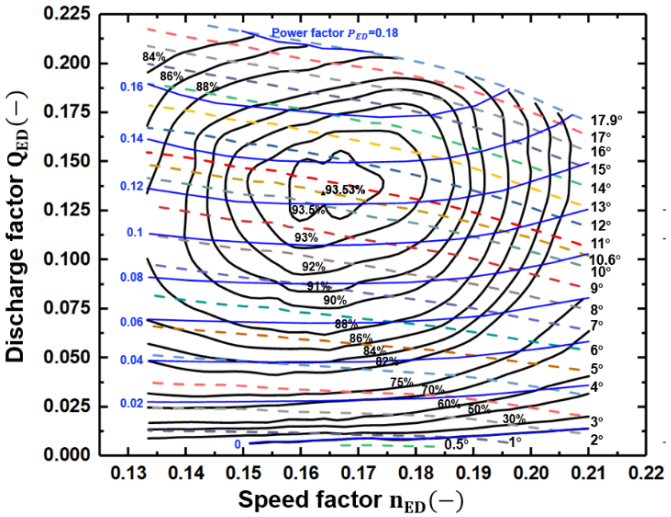

Figure 7. The Hill chart of the reduced-scale Francis turbine: GVOs α as a function of speed factor n_{ED} (Equation (11)), discharge factor Q_{ED} (Equation (12)) and power factor P_{ED} (Equation (13)). Model test head is 22–62 m. The Reynolds number is equal to 7×10^6. The water temperature is 20 °C.

Figure 8 shows the operating characteristic curves of the prototype generated by scaling up the experimental results of the model turbine, the constant speed is attained by regulating the gate opening, thereby varying the discharge flowing through the turbine as the load varies. Twenty-four operating points were selected to verify the validity of the chart. The fewer deviations between this Hill chart and data in witness test confirm the validity of Hill diagram to characterize the energy performance of prototype turbine. It shows that the prototype machine can operate up to 94.75% efficiency in more than 1/3 operating space between 16–20.5 m^3/s flow rate and 576–690 m net head, indicating a wide optimum operating region. The high-efficiency area becomes relatively narrow during the water head ranging from 640 to 650 m. The power output of the turbine displays enormous sensitivity to the discharge as shown in power contours. One cubic meter variation in flow rate will result in a 10MW-level power fluctuation, which should draw attention to power station regulation.

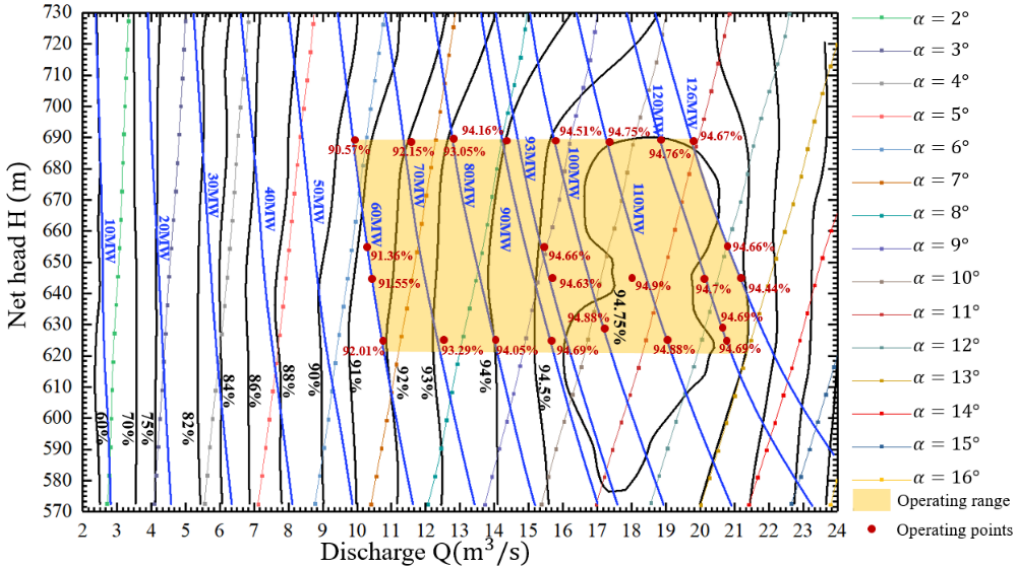

Figure 8. The calculated real-scale prototype Hill diagram. Red dots represent twenty-four verification points of the prototype turbine in witness experiment with a constant runner speed of 600 rpm and water temperature of 18 °C.

3.2.2. Pressure Pulsations

Pressure pulsations were studied based on the time-series pressure signals measured by sensor network in Figure 2. Fifty-seven operating cases were performed under a broad GVOs range from 0.47° to 18° at n_{ED} = 0.158, 0.164, and 0.166, respectively. The pressure pulsations were displayed both as root-mean-square (RMS) and peak-to-peak values with 97% confidence in Equation (20). All pressure data was performed spectral analysis to reveal frequency components and their amplitudes.

$$\left(\frac{\Delta H}{H}\right)_{rms} = \sqrt{\left[\frac{1}{n}\sum_{i=1}^{n}\left(\frac{\Delta H_i}{H}\right)^2\right]} \tag{20}$$

where ΔH is the pressure amplitude with 97% reliability in the time domain, H is the turbine head. n is the number of samples used to estimate RMS.

The spectral analysis of three n_{ED} conditions shows the same trend and characteristics. Finally, the pressure signals at n_{ED} = 0.164 were selected to discuss the pressure fluctuations. Figure 9 shows the dimensionless peak-to-peak values of pressure fluctuations ($\Delta H/H$) with respect to the gate openings. The domain was categorized into the five regions within the whole experimental range according to the amplitude characteristics of pressure fluctuations.

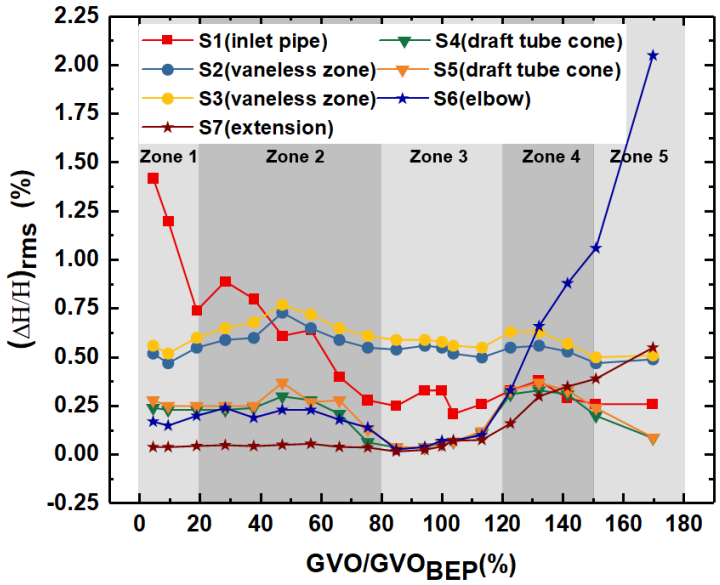

Figure 9. Non-dimensional peak-to-peak values of pressure pulsations with GVOs variations (from 4% to 170% of GVO_{BEP}) at seven measured locations, where GVO_{BEP} represents the GVOs with 10.6° at $n_{ED} = 0.164$, where the turbine achieves the best efficiency.

In Zone 1 defined as DPL operation (0.04–0.2 GVO_{BEP}), the highest amplitude of pressure fluctuations from sensor S1 is about three times of that in vaneless space at GVOs = 0.47°, reaching 1.42% of net head, while it ramps down to 0.74% head when gate opening is increased by 1.53°. This severe vibration in inlet pipe is probably related to the natural frequency of hydraulic system. The minimal pressure pulsation occurs in draft tube extension corresponding to the sensor S7. In general, pressure pulsations in Zone 1 are extremely low except for the turbine inlet. However, the turbine will perform with low hydraulic efficiency under such a small flow rate (Figure 7), a huge stagnant area of fluid makes it impossible for the turbine to operate in this area for a long time. In Zone 2, corresponding to PL operation (0.2–0.8 GVO_{BEP}), the pressure amplitudes increase first and then decreases slowly with the discharge increase. The maximum occurs around 0.5 GVO_{BEP}, which is consistent with the literature [44,45] before. Therefore, 50% of GVO_{BEP} should be avoided as much as possible when the turbine is operated with a low load. The pressure signals of sensor S7 show the smaller amplitudes and fluctuations than the other six sensors. All pressure pulsations trend to be minimized in Zone 3 with the GVOs around BEP within ±10% deviation. The main pulsations originate from the vaneless space. In Zone 4 defined as HL operation, the amplitudes suddenly increase 15-fold from BEP at elbow compared with 5.42 times at tube extension. Whereas, the other pressure amplitudes show an inverted V-shaped trend with a peak oscillation at 1.3 GVO_{BEP}. In this zone, the amplitude difference between runner upstream (vaneless space) and downstream (draft tube) is significantly reduced due to the damping effect of water. When the turbine works under FL conditions from 1.5–1.7 GVO_{BEP}, the vibrations in elbow and rectangular diffuser continue to deteriorate, which increases by 28 times and 12 times as compared with that in BEP configuration, respectively. The most significant pressure fluctuations occurs in the draft tube bend with more than 2.05% head throughout the whole operated period. This potential risk may reduce the margin for safe operation of power stations. The vaneless space produces the relatively stable pressure fluctuation but with a high amplitude between 0.47–0.77% of the net head. There is no obvious amplitude difference in S4 and S5 due to the same pulsation energy when the pressure fluctuation propagates to the same cross-section in the draft tube.

The frequency spectrums of pressure data are presented in Table 4. The runner frequency f_n equals to the runner rotational speed in revolutions per second, as calculated according to the Equation (21). The blade passing frequency f_b is observed in two pressure sensors S2 and S3 for all investigated cases, showing that the pressure field at the vaneless space is strongly influenced by the interactions between

the stationary guide vanes and the rotating runner blades. The blade passing frequency depends on the runner rotational speed f_n and the number of blades Z_b, as shown in Equation (22). A low harmonic frequency 0.5 f_b and a high harmonic frequency 2 f_b can be observed at all operating conditions, it indicates that the pressure fluctuations originated in the available space between the runner and guide vanes spread throughout the fluid domain, upstream to the inlet pipe and downstream to the draft tube outlet

$$f_n = \frac{n}{60} \tag{21}$$

$$f_b = Z_b f_n \tag{22}$$

Table 4. The dominant frequency of seven monitoring sites.

GVO	Dominant Frequency							f_b (HZ)	n (rpm)
	S1	S2	S3	S4	S5	S6	S7		
0.47	3.3	327	327	3.1	3.1	3.5	3.3	326.9	653.8
1	3.5	327	327	3.3	3.1	4.6	14.7	327.5	645.9
2	3.7	328	329	3.1	3.3	3.5	3.5	327.7	655.3
3	3.3	327	327	3.5	3.5	3.7	3.7	327.3	654.7
4	3.1	327	327	11.7	13	3.7	3.5	327.4	654.7
5	4	327	327	3.3	3.3	3.7	3.5	327.3	654.5
6	3.5	327	327	3.3	3.3	3.5	3.5	327.2	654.4
7	3.7	327	327	3.3	3.3	4	3.7	327.4	654.7
8	3.7	327	327	4.4	3.3	3.7	3.5	327.4	654.8
9	3.5	327	327	11.2	0.001	0.001	11.2	327.4	654.7
10	3.3	327	327	4.4	4.4	3.5	3.3	327.2	654.4
10.6	3.3	331	331	4.2	4.2	3.5	3.5	331	662
11	3.5	327	327	5.1	5.1	4.4	3.7	327.4	654.7
12	3.3	327	327	3.1	3.1	3.1	3.3	327.3	654.6
13	3.3	327	327	3.1	3.1	3.3	19.4	327.4	654.8
14	3.5	327	327	3.5	3.5	4.8	23.1	327.3	654.7
15	3.3	319	319	3.5	3.5	8.6	16.1	318.6	637.2
16	3.3	319	319	3.5	3.5	8.4	18.3	318.7	637.3
18	4	307	307	154	154	5.1	21.8	307.2	614.5

The pressure sensor S1 is integrated in the turbine inlet connected to the pressure tank, producing the standing waves. A. Favrel et al. [45] measured the pressure signal in the feeding pipe of a reduced-scale Francis turbine and found that the precession frequency remains at 0.26–0.36 times of the runner frequency for discharge values between 50% and 85% of the BEP. Our analysis shows that the frequency of pipe inlet changes less with the varied GVOs, between 0.28–0.39 times of the runner frequency from DPL to FL conditions. The surging effect in the conduit may be to blame for this kind of low-frequency fluctuation. The frequency distribution in the draft tube is complex, which might be associated with the vortex rope. The frequency of the S4 and S5 is almost the same, except for the obvious difference at 9°, where S4 and S7 with both 11.2 HZ, S5 and S6 with 0.001 HZ, indicating that the frequency produced in draft tube cone is propagated downstream. At 4° and 10.6°, the frequency of S4 equals about 1.07 and 0.93 times of the runner frequency. The same phenomenon is captured for S5, with 1.19 and 0.93 times the runner frequency. In the high flow rate at 1.7 GVO_{BEP}, the medium frequency 154 HZ occurs first in the whole range of the investigated operating conditions, about 0.5 times the blade frequency. The frequency of S6 and S7 is basically within the range of 0.3–0.4 times the runner speed at part load condition, while changes to 0.8–2 times at full load condition.

The vortex rope downstream the runner gives an obvious impacts on the Francis turbine performance at low discharge conditions through inducing the pressure fluctuations and hydraulic oscillations in draft tube cone. Figure 10 presents the varying shapes of vortex ropes at different load. The pattern and behavior of vortex rope are observed to vary with the discharge conditions. A helical structure of vortex rope originated from the runner hub is observed at the very low discharged condition of the turbine in Figure 10a,b. The rotation direction is the same as that of the runner. The whole vortex

band develops to the end of the straight cone and has obvious eccentricity. As the operating point moves towards BEP, the eccentricity and diameter of the vortex band decrease. No swirling of flow at runner downstream occurs at BEP condition as shown in Figure 10c. A spindle vortex occurs at the cone center under HL condition in Figure 10d with the opposite direction of rotation to the runner. The axisymmetric cavitation vortex belt gradually intensifies as load increases.

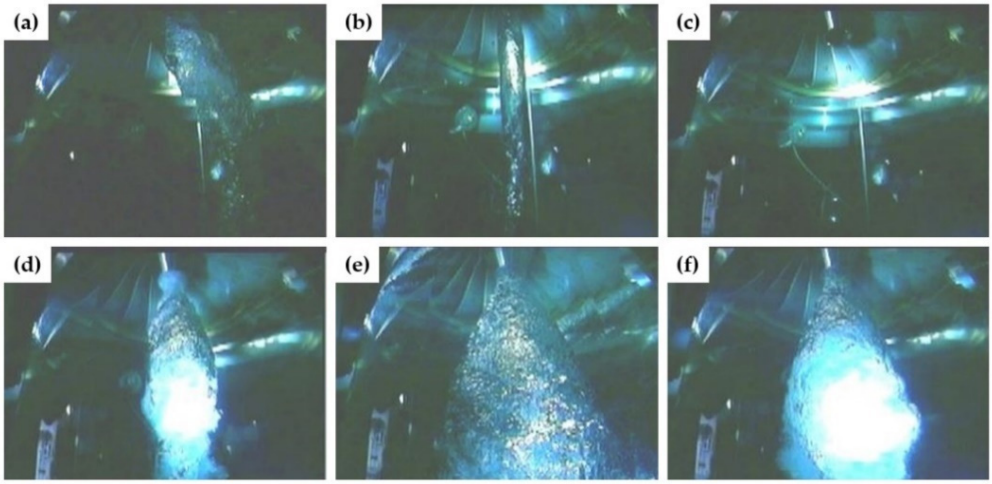

Figure 10. Varying shapes of vortex ropes at different loads (flow rate). (**a**) P_{mP} = 60 MW; (**b**) P_{mP} = 80 MW; (**c**) P_{mP} = 100 MW; (**d**) P_{mP} = 120 MW; (**e**) P_{mP} = 124 MW; (**f**) P_{mP} = 126 MW.

3.2.3. Guide Vane Torque

The unit is vulnerable under the runaway condition. According to the long-term experience in China, designing the guide vanes with a self-close function is a reliable method to avoid the runaway. The guide vane torque (GVT) on the distributor in synchronized and desynchronized mode is an essential reference for preliminary design stage. Therefore, the relative measurements were performed on dedicated guide vane shafts of the model turbine at various GVOs from 0.5° to 18°. The lowest and highest water head of 625 m and 690 m in operation regime were investigated.

Figure 11 depicts the variation in the GVT under synchronized conditions. The positive and negative values represent the opening and closing direction, respectively. Under the same discharge, the torque of five different guide vanes is basically the same, demonstrating a uniform torque distribution at 23 guide vanes. Under varied discharges, the trend of each GVT varying with the GVOs is similar. The whole zone can be divided into three parts. Before GVOs < 1°, the torque is a positive value. In this zone, as the GVOs increase, the torque decreases and changes towards the opposite direction. When 1° < GVOs < 13°, the torque becomes a negative value. The torque almost decreases linearly with the GVOs increment. When GVOs > 13°, the torque no longer declines significantly. The GVT proves a great self-closing performance of the designed guide vanes during the whole change process of GVOs. The torque of guide vane 23# shown in Figure 11c indicates that a greater water head results in a larger torque (absolute value) at the same GVOs, and the torque difference increases as the GVOs rise, the largest gap occurs at GVOs = 18°, with about 1 kN·m.

For the desynchronized configurations, the measurements were carried out under the fixing misaligned guide vanes (MGVs) and varying the other synchronized vanes from 0.5° to 18°, as shown in Figure 12. Four positions of the aligned guide vane 11#,12# and 13# are located at 0.5°, 8°, 12°, and 18°, respectively. The torque of three guide vanes differs a lot, except for the synchronization, where the MGVs rotate to the same angle as the synchronous guide vanes. All torque curves approach toward the synchronization from the starting position and then away with a constant slope in the whole negative zone, which presents a satisfactory self-closing capability. The absolute torque value at the low head is larger than that of the high head under the same GVOs except for GVOs = 0.5°.

Compared with the synchronous conditions, the maximum absolute value of torque is at least doubled. Although MGVs have been proven to be an effective measure to improve flow stability and minimize pressure pulsations, the large torque value should be the focus during the design, which may be a limitation of such technology.

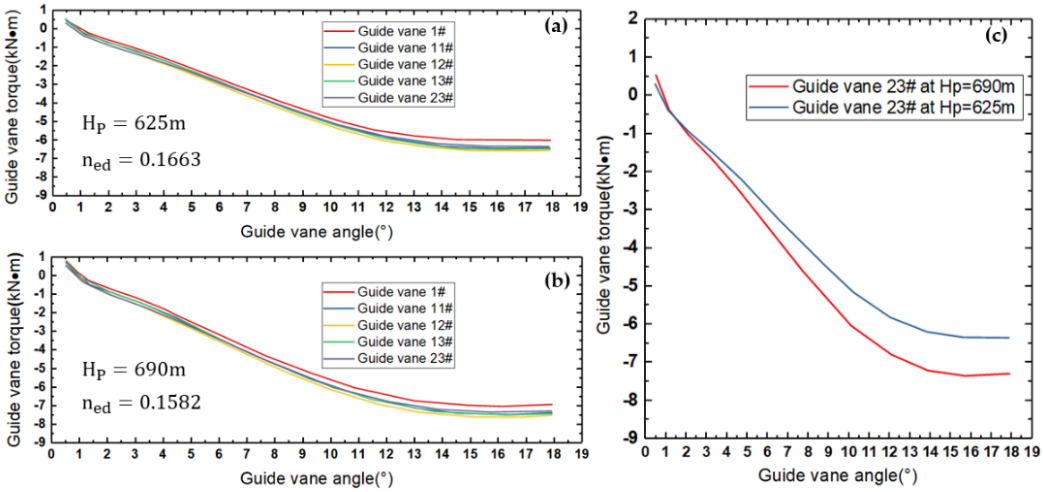

Figure 11. Prototype GVT measured on guide vane 1#, 11#, 12# and 23# under aligned conditions with runner speed of 600 rpm, (**a**) at minimum head 625 m; (**b**) at maximum head 690 m; (**c**) the measured torque of guide vane 23# at minimum head 625 m and maximum head 690 m, respectively.

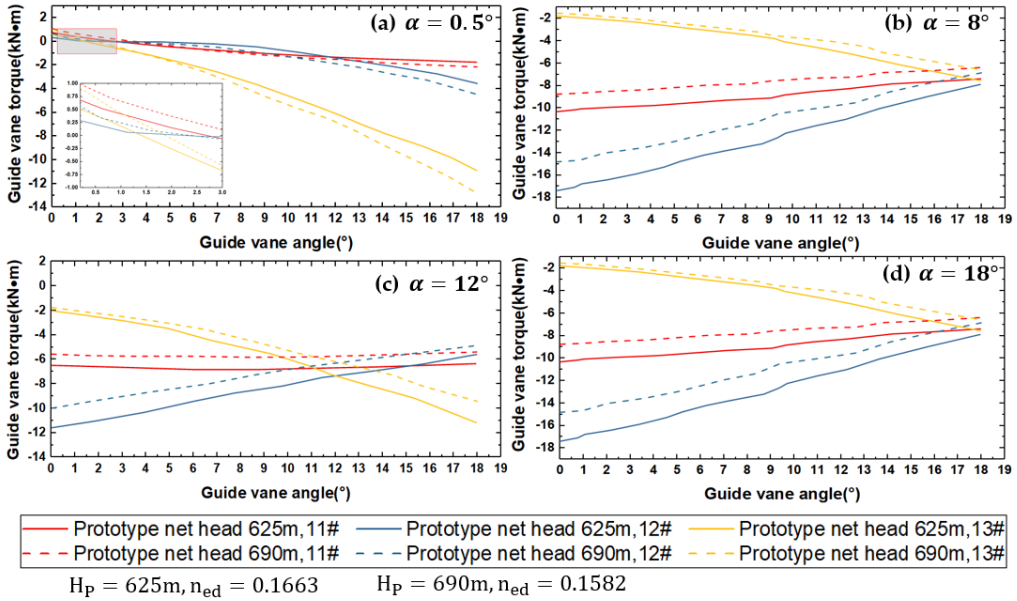

Figure 12. The prototype GVT under misaligned conditions varies with GVOs under H_P = 625 m and 690 m.(**a**) 11#,12# and 13# guide vanes with 0.5° GVOs, (**b**) 11#,12# and 13# guide vanes with 8° GVOs, (**c**) 11#,12# and 13# guide vanes with 12° GVOs, (**d**) 11#,12# and 13# guide vanes with 18° GVOs.

4. Conclusions

With the rapid growth of hydropower worldwide, the large-scale high-head Francis turbines have become a research hotspot. In this study, a super high-head Francis turbine with a gross head of nearly 700 m was designed with CFD simulation and laboratory tests. The performance of the designed super high-head Francis turbine was investigated under variable discharge conditions using a numerical and experimental approach. The following are the findings based on the present work.

The CFD-based technique is proven as an effective tool to predict the flow characteristics like velocity profiles and pressure distribution, which is significant to developing new designs and improving existing design of hydraulic machines. The CFD analysis demonstrates a strong rotor–stator interaction between guide vanes and runner blades as a result of the high-speed tangential flow towards runner created by the super high water head and the small gap between the radial blades. Only minor energy loss occurs at the trailing edge of stay vanes and guide vanes. The experiment was conducted to investigate the performance of the reduced scale runner model (1:3.7), including operating characteristics, pressure fluctuations and guide vane torque. The calculated real-scale prototype hill diagram shows that BEP is located at GVOs = 10.6°, and the hydraulic efficiency is 94.75% at the nominal condition. The pressure signals were collected by a sensor network at various locations. The pressure variation at the vaneless space is more stable than that at the pipe inlet and draft tube elbow, where the two largest vibrations are observed at deep part-load and full load, reaching 1.42% and 2.05% of $\Delta H/H$, respectively. Therefore, additional attentions should be paid to the inlet pipe and elbow when designing the super high-head turbines. The spectrum analysis reveals that blade passing frequency is the main component in vaneless space, where the strong rotor–stator interaction occurs. The low frequency is observed in the inlet pipe and draft tube within the 0.26–0.36 times of the runner speed. The behavior of vortex rope varies from a swirling flow at part-load condition to a spindle vortex structure at high-load condition. The guide vane torque measured in synchronized and misaligned configurations shows that the design guide vanes have a great self-closing ability, which proved to be an effective method to avoid dangerous runaway. Under synchronized conditions from DPL to FL, all guide vane torques show the similar variation trend with fewer value gap. They decrease first and then keep relatively stable at HL. However, the torque of adjacent MGVs differs a lot, except at the synchronous GVOs at misaligned conditions. The maximum absolute value of torque is at least doubled compared to that in synchronized configurations, which may be a potential hazard for the MGVs' application.

Author Contributions: Z.T. and H.L.: Conceptualization, Methodology, writing; J.M. and Y.Z.: Project administration; S.T., Q.C. and Y.L.: Writing—Reviewing and Editing. All authors have read and agreed to the published version of the manuscript.

Funding: This work was supported by the National Natural Science Foundation (51821093), Zhejiang Provincial Natural Science Foundation (LR19E050002), Zhejiang Province Key Science and Technology Project (2019C01057).

Conflicts of Interest: The authors declare no conflict of interest.

References

1. Muhirwa, A.; Cai, W.; Su, W.; Liu, Q.; Binama, M.; Li, B.; Wu, J. A review on remedial attempts to counteract the power generation compromise from draft tubes of hydropower plants. *Renew. Energy* **2020**, *150*, 743–764. [CrossRef]
2. Breeze, P. *Hydropower*; Academic Press: London, UK, 2018.
3. Li, X.; Chen, Z.; Fan, X.; Cheng, Z. Hydropower development situation and prospects in China. *Renew. Sustain. Energy Rev.* **2018**, *82*, 232–239. [CrossRef]
4. Trivedi, C.; Agnalt, E.; Dahlhaug, O.G. Investigations of unsteady pressure loading in a Francis turbine during variable-speed operation. *Renew. Energy* **2017**, *113*, 397–410. [CrossRef]
5. Dörfler, P.; Bloch, R.; Mayr, W.; Hasler, O. Vibration tests on a high-head (740 m) Francis turbine: Field test results from Hausling. In Proceedings of the 14th IAHR Symposium on Hydraulic Machinery and Cavitation, Trondheim, Norway, 20–23 June 1988; Desbaillets, J., Ed.; TAPIR Publ: Trondheim, Norway, 1988; pp. 241–252.
6. Ma, Z.; Zhu, B.; Rao, C.; Shangguan, Y. Comprehensive hydraulic improvement and parametric analysis of a Francis turbine runner. *Energies* **2019**, *12*, 307. [CrossRef]
7. Zhang, Q.; Tong, Z.; Tong, S. Effect of cathode recirculation on high potential limitation and self-humidification of hydrogen fuel cell system. *J. Power Sources* **2020**, *468*, 228388. [CrossRef]

8. Tong, Z.; Wu, S.; TONG, S.; Yue, Y.; Li, Y.; Xu, Z.; Zhong, Y. Energy-saving technologies for construction machinery: A review of electro-hydraulic pump-valve coordinated system. *J. Zhejiang Univ. Sci. A* **2020**, *21*, 331–349. [CrossRef]
9. Yu, A.; Zou, Z.; Zhou, D.; Zheng, Y.; Luo, X. Investigation of the correlation mechanism between cavitation rope behavior and pressure fluctuations in a hydraulic turbine. *Renew. Energy* **2020**, *147*, 1199–1208. [CrossRef]
10. Tong, Z.; Xin, J.; Tong, S.; Yang, Z.; Zhao, J.; Mao, J. Internal flow structure, fault detection, and performance optimization of centrifugal pumps. *J. Zhejiang Univ. Sci. A* **2020**, *21*, 85–117. [CrossRef]
11. Tong, Z.; Liu, H. Modeling In-Vehicle VOCs Distribution from Cabin Interior Surfaces under Solar Radiation. *Sustainability* **2020**, *12*, 5526. [CrossRef]
12. Tong, Z.; Li, Y. Real-Time Reconstruction of Contaminant Dispersion from Sparse Sensor Observations with Gappy POD Method. *Energies* **2020**, *13*, 1956. [CrossRef]
13. Kavurmaci, B.; Celebioglu, K.; Aradag, S.; Tascioglu, Y. Model Testing of Francis-Type Hydraulic Turbines. *Meas. Control.* **2017**, *50*, 70–73. [CrossRef]
14. Litvinov, I.; Shtork, S.; Gorelikov, E.; Mitryakov, A.; Hanjalic, K. Unsteady regimes and pressure pulsations in draft tube of a model hydro turbine in a range of off-design conditions. *Exp. Fluid Sci* **2018**, *91*, 410–422. [CrossRef]
15. Laouari, A.; Ghenaiet, A. Predicting unsteady behavior of a small francis turbine at several operating points. *Renew. Energy* **2019**, *133*, 712–724. [CrossRef]
16. Zhang, Y.; Chen, T.; Li, J.; Yu, J. Experimental study of load variations on pressure fluctuations in a prototype reversible pump turbine in generating mode. *ASME J. Fluids Eng.* **2017**, *139*, 74501. [CrossRef]
17. Tong, Z.; Cheng, Z.; Tong, S. Preliminary design of multistage radial turbines based on rotor loss characteristics under variable operating conditions. *Energies* **2019**, *12*, 2550. [CrossRef]
18. Goyal, R.; Gandhi, B.K. Review of hydrodynamics instabilities in Francis turbine during off-design and transient operations. *Renew. Energy* **2018**, *116*, 697–709. [CrossRef]
19. Li, D.; Sun, Y.; Zuo, Z.; Liu, S.; Wang, H.; Li, Z. Analysis of pressure fluctuations in a prototype pump-turbine with different numbers of runner blades in turbine mode. *Energies* **2018**, *11*, 1474. [CrossRef]
20. Wu, Y.; Liu, S.; Dou, H.; Wu, S.; Chen, T. Numerical prediction and similarity study of pressure fluctuation in a prototype Kaplan turbine and the model turbine. *Comput. Fluids* **2012**, *56*, 128–142. [CrossRef]
21. Müller, A.; Favrel, A.; Landry, C.; Avellan, F. Fluid–structure interaction mechanisms leading to dangerous power swings in Francis turbines at full load. *J. Fluid Struct* **2017**, *69*, 56–71. [CrossRef]
22. Devals, C.; Vu, T.C.; Guibault, F. CFD analysis for aligned and misaligned guide vane torque prediction and validation with experimental data. *Int. J. Fluid Mach. Syst.* **2015**, *8*, 132–141. [CrossRef]
23. Vu, T.; Koller, M.; Gauthier, M.; Deschênes, C. Flow simulation and efficiency hill chart prediction for a Propeller turbine. *Int. J. Fluid Mach. Syst.* **2011**, *4*, 243–254. [CrossRef]
24. Trivedi, C.; Cervantes, M.J.; Dahlhaug, O.G. Experimental and numerical studies of a high-head Francis turbine: A review of the Francis-99 test case. *Energies* **2016**, *9*, 74. [CrossRef]
25. Arpe, J.; Nicolet, C.; Avellan, F. Experimental evidence of hydroacoustic pressure waves in a Francis turbine elbow draft tube for low discharge conditions. *ASME J. Fluids Eng.* **2009**, *131*, 081102. [CrossRef]
26. Alligné, S.; Maruzewski, P.; Dinh, T.; Wang, B.; Fedorov, A.; Iosfin, J.; Avellan, F. Prediction of a Francis turbine prototype full load instability from investigations on the reduced scale model. *IOP Conf. Ser. Earth Environ. Sci.* **2010**. [CrossRef]
27. Nicolle, J.; Morissette, J.; Giroux, A. Transient CFD simulation of a Francis turbine startup. *IOP Conf. Ser. Earth Environ. Sci.* **2012**. [CrossRef]
28. Choi, H.-J.; Zullah, M.A.; Roh, H.-W.; Ha, P.-S.; Oh, S.-Y.; Lee, Y.-H. CFD validation of performance improvement of a 500 kW Francis turbine. *Renew. Energy* **2013**, *54*, 111–123. [CrossRef]
29. Minakov, A.; Platonov, D.; Dekterev, A.; Sentyabov, A.; Zakharov, A. The numerical simulation of low frequency pressure pulsations in the high-head Francis turbine. *Comput. Fluids* **2015**, *111*, 197–205. [CrossRef]
30. Teran, L.A.; Larrahondo, F.J.; Rodríguez, S.A. Performance improvement of a 500-kW Francis turbine based on CFD. *Renew. Energy* **2016**, *96*, 977–992. [CrossRef]
31. Trivedi, C.; Cervantes, M.J.; Gandhi, B. Investigation of a high head Francis turbine at runaway operating conditions. *Energies* **2016**, *9*, 149. [CrossRef]

32. Doujak, E.; Eichhorn, M. An approach to evaluate the lifetime of a high head francis runner. In Proceedings of the 16th International Symposium on Transport Phenomena and Dynamics of Rotating Machinery, Honolulu, HI, USA, 10–15 April 2016.
33. Anup, K.; Lee, Y.H.; Thapa, B. CFD study on prediction of vortex shedding in draft tube of Francis turbine and vortex control techniques. *Renew. Energy* **2016**, *86*, 1406–1421.
34. Conrad, P.; Weber, W.; Jung, A. Deep Part Load Flow Analysis in a Francis Model turbine by means of two-phase unsteady flow simulations. *J. Phys. Conf. Ser.* **2017**, *813*, 012027. [CrossRef]
35. Yamamoto, K. Hydrodynamics of Francis Turbine Operation at Deep Part Load Condition. Ph.D. Thesis, Ecole Polytechnique Fédérale de Lausanne (EPFL), Lausanne, Switzerland, 2017.
36. Eichhorn, M.; Taruffi, A.; Bauer, C. Expected load spectra of prototype Francis turbines in low-load operation using numerical simulations and site measurements. *J. Phys. Conf. Ser.* **2017**, *813*, 012052. [CrossRef]
37. Decaix, J.; Hasmatuchi, V.; Titzschkau, M.; Münch-Alligné, C. CFD Investigation of a high head Francis turbine at speed no-load using advanced URANS models. *Appl. Sci.* **2018**, *8*, 2505. [CrossRef]
38. Pasche, S.; Gallaire, F.; Avellan, F. Origin of the synchronous pressure fluctuations in the draft tube of Francis turbines operating at part load conditions. *J. Fluid Struct* **2019**, *86*, 13–33. [CrossRef]
39. Unterluggauer, D.-I.J. Investigations on Critical Low-Load and Transient Operation of a Prototype Francis Turbine. Ph.D. Thesis, Austrian Institute of Technology, Vienna, Austria, 2019.
40. Goyal, R.; Gandhi, B.K.; Cervantes, M.J. PIV measurements in Francis turbine–a review and application to transient operations. *Renew. Sustain. Energy Rev.* **2018**, *81*, 2976–2991. [CrossRef]
41. International Electrotechnical Commission. Hydraulic turbines, storage pumps and pump-turbines: Model acceptance tests. In *International Standard*; IEC 60193; International Electrotechnical Commission: Geneva, Switzerland, 1999; p. 578.
42. International Organization for Standardization. Measurement of Liquid Flow in Closed Conduits–Weighing Method. In *International Standard*; ISO 4185; International Organization for Standardization: Geneva, Switzerland, 1980.
43. Aggidis, G.A.; Židonis, A. Hydro turbine prototype testing and generation of performance curves: Fully automated approach. *Renew. Energy* **2014**, *71*, 433–441. [CrossRef]
44. Tong, Z.; Whitlow, T.H.; MacRae, P.F.; Landers, A.J.; Harada, Y. Quantifying the effect of vegetation on near-road air quality using brief campaigns. *Environ. Pollut.* **2015**, *201*, 141–149. [CrossRef]
45. Favrel, A.; Müller, A.; Landry, C.; Yamamoto, K.; Avellan, F. Study of the vortex-induced pressure excitation source in a Francis turbine draft tube by particle image velocimetry. *Exp. Fluids* **2015**, *56*, 215. [CrossRef]